Science Advances
AAAS

advances.sciencemag.org/cgi/content/full/5/7/eaaw5296/DC1

Supplementary Materials for

Battery-free, fully implantable optofluidic cuff system for wireless optogenetic and pharmacological neuromodulation of peripheral nerves

Yi Zhang, Aaron D. Mickle, Philipp Gutruf, Lisa A. McIlvried, Hexia Guo, Yixin Wu, Judith P. Golden, Yeguang Xue, Jose G. Grajales-Reyes, Xueju Wang, Siddharth Krishnan, Yiwen Xie, Dongsheng Peng, Chun-Ju Su, Fengyi Zhang, Jonathan T. Reeder, Sherri K. Vogt, Yonggang Huang, John A. Rogers*, Robert W. Gereau IV*

*Corresponding author. Email: jrogers@northwestern.edu (J.A.R.); gereaur@wustl.edu (R.W.G.)

Published 5 July 2019, *Sci. Adv.* **5**, eaaw5296 (2019)
DOI: 10.1126/sciadv.aaw5296

The PDF file includes:

Other Supplementary Material for this manuscript includes the following:

(available at advances.sciencemag.org/cgi/content/full/5/7/eaaw5296/DC1)

Movie S1 (.mp4 format). The deformation of the flexible membrane.
Movie S2 (.mp4 format). The flow of fluid from the reservoir.
Movie S3 (.mp4 format). Mouse with a blue μ-LED during exercise on a running wheel.

Note S1. Pressure in the pump chamber and drug reservoir.

To quantitatively predict the pressure in the pump chamber and drug reservoir, an analytical model is established for the whole pump system.

Ideal gas law of the pump chamber gives

$$P(V + V_0) = nRT \quad \text{(Eq S1)}$$

where P is the pressure, V_0 and V are the initial volume and volume change of air inside the pump chamber, respectively, n is the number of moles of air, R is the ideal gas constant, and T the temperature.

The rate form of Eq S1 is,

$$\dot{P}(V + V_0) + P\dot{V} = \dot{n}RT \quad \text{(Eq S2)}$$

where the gas generation rate $\dot{n}$ can be related to the effective current i by

$$\dot{n} = \frac{3i}{4F} \quad \text{(Eq S3)}$$

and F is the Faraday's constant. It's worth noting here that volume increase V in the pump chamber is just the volume of drug delivered such that $\dot{V}$ is the flow rate Q.

The pressure difference between the water-split chamber and atmosphere pressure $P - P_0$ is due to (1) the flow resistance in microfluidic channel $P_{drug} - P_0$, and (2) the resistance from the stiffness of the flexible membrane $P - P_{drug}$. Finite element analysis of the flexible membrane gives the relationship between volume increase of the pump chamber V and pressure difference in pump chamber and drug reservoir $P - P_{drug}$ as

$$P - P_{drug} = f(V) \quad \text{(Eq S4)}$$

Three-dimensional solid elements (C3D8R in ABAQUS finite element software) are used for the flexible membrane and the contact between flexible membrane and reservoir walls/covers are considered in the simulation. The flow resistance induced pressure change $P_{drug} - P_0$ can be obtained from Poiseuille's law as

$$P_{drug} - P_0 = \frac{32\mu L\dot{V}}{w^4} \quad \text{(Eq S5)}$$

where w and L are the width (the height is the same as the width) and length of the delivery channel, and μ is the viscosity of the drug.

Combining Eq S2, Eq S4 and Eq S5, the differential equation of the system is given by

$$\left[\frac{32\mu L}{w^4}\ddot{V} + f'(V)\dot{V}\right](V + V_0) + \left[\frac{32\mu L}{w^4}\dot{V} + f(V) + P_0\right]\dot{V} = \dot{n}RT \quad \text{(Eq S6)}$$

The numerical solution to the above under initial conditions $V(t = 0) = 0$, and $\dot{V}(t = 0) = 0$ gives the delivered drug volume V and flow rate $Q = \dot{V}$ versus time. The pressure in pump chamber and drug reservoir are solved accordingly using Eq S4 and Eq S5.

Note S2. Models for the radius of the cuff.

As described above, the cuff is made by results from bonding a pre-strained film (initial thickness t, initial length L_1, pre-strain χ) of PDMS to a film without pre-strain [thickness t, initial length $L_2 = (1+\chi)L_1$] and then releasing the pre-strain (fig. S8). The result yields an arc shape with an angle α, where the bending radius from the center of the arc to the interface of the two bonded strips is denoted by R_0 (corresponding curvature κ_0). Let y define the coordinate along the thickness direction, with $y = 0$ at the interface of the two bonded films. According to Euler beam theory and linear elastic constitutive relations, the axial stress distribution in the top pre-stretched and bottom non-stretched films can be given by

$$\sigma_1 = E_{PDMS}\left(\frac{R_0\alpha + y\alpha}{L_1} - 1\right)$$

$$\sigma_2 = E_{PDMS}\left(\frac{R_0\alpha + y\alpha}{L_2} - 1\right) \qquad \text{(Eq S7)}$$

Mechanical equilibrium requires that the net forces and moments are zero, yielding

$$\int_0^t \sigma_1 dy + \int_{-t}^0 \sigma_2 dy = 0$$

$$\int_0^t \sigma_1 y dy + \int_{-t}^0 \sigma_2 y dy = 0 \qquad \text{(Eq S8)}$$

Combining Eq S7 and Eq S8 gives

$$R_0 = \frac{4+2\chi}{3\chi}t \qquad \text{(Eq S9)}$$

The inner radius of the cuff is thus given by

$$R_{inner} = R_0 - t = \frac{4-\chi}{3\chi}t \qquad \text{(Eq S10)}$$

In other words, the critical pre-strain required for a bi-layer cuff to surround a nerve with radius R_{nerve} is given by

$$\chi_{cr} = \frac{4t}{3R_{nerve}+t} \quad \text{(Eq S11)}$$

Note S3. Analytical model of contact pressure between the nerve and the cuff.

An analytical model yields estimates of the average contact pressure between the nerve and the cuff. In practical applications, the applied pre-strain χ is typically slightly larger than the critical value χ_{cr}. As a result, the inner radius of the resulting cuff R_{inner} is slightly smaller than the nerve radius R_{nerve}, such that modest contact pressure appears at the interface. The literature value of the modulus of peripheral nerve tissue is ~7 MPa. For the range of parameters of interest here, FEA shows that the nerve barely deforms after contact with PDMS cuff (3 MPa), and thus can be considered as rigid in this analysis (fig. S9B).

The analysis starts with determination of the average curvature of the cuff after applying a uniform pressure P. The cuff is assumed to fit the nerve when its average curvature (inner side) is equal to that of the nerve. The equilibrium equations for the cuff under pressure P are given by

$$\int_0^t \sigma_1 dy + \int_{-t}^0 \sigma_2 dy = 0$$

$$\int_0^t \sigma_1 y dy + \int_{-t}^0 \sigma_2 y dy = M(\theta) \quad \text{(Eq S12)}$$

The stresses σ_1 and σ_2 in Eq S12 are given by

$$\sigma_1 = E_{PDMS}\left[\frac{R_0{}'\alpha + y\alpha}{L_1} - 1\right]$$

$$\sigma_2 = E_{PDMS}\left[\frac{R_0{}'\alpha + y\alpha}{L_2} - 1\right] \quad \text{(Eq S13)}$$

And the bending moment $M(\theta)$ from uniform pressure P is given by

$$M(\theta) = -\int_0^\theta R_0 \sin\xi \, PR_0 d\xi = PR_0^2(\cos\theta - 1) \quad \text{(Eq S14)}$$

Solving the combined equations of Eq S12 and Eq S13 gives the radius of the cuff (at the bonding interface between the pre-strained and non-pre-strained films) after applying pressure as

$$R_0'(\theta) = t\left[\frac{\frac{M(\theta)}{Et^2}3\chi+8+4\chi}{\frac{M(\theta)}{Et^2}(12+6\chi)+6\chi}\right] \quad \text{(Eq S15)}$$

And the inner radius of the cuff is given by

$$R_{inner}'(\theta) = R_0'(\theta) - t = t\left[\frac{8-\frac{M(\theta)}{Et^2}(12+3\chi)-2\chi}{\frac{M(\theta)}{Et^2}(12+6\chi)+6\chi}\right] \quad \text{(Eq S16)}$$

To fit the nerve requires that the average inner radius is equal to the nerve radius R_{nerve}

$$\overline{R_{inner}'(\theta)} = \frac{1}{\alpha}\int_0^\alpha t\left[\frac{8-\frac{M(\theta)}{Et^2}(12+3\chi)-2\chi}{\frac{M(\theta)}{Et^2}(12+6\chi)+6\chi}\right]d\theta = R_{nerve} \quad \text{(Eq S17)}$$

The required pressure P can be solved numerically from Eq S17, which depends on the pre-strain χ, the arc angle of formed cuff, and the normalized nerve radius R_{nerve}/t:

$$\frac{P}{E_{PDMS}} = \psi\left(\chi, \alpha, \frac{R_{nerve}}{t}\right) \quad \text{(Eq S18)}$$

Note S4. Oxygen and hydrogen permeability of the flexible SBS membrane.

Gas permeation across flexible SBS membranes is measured via an isochoric (constant volume, varying pressure) gas permeation system as shown in fig. S13. The isochoric permeation system is enclosed in an incubator at 35 °C. Prior to each measurement, the whole system is evacuated to 10 mTorr for 12 hours in order to get rid of trapped gases. At the beginning of each measurement, the feed side is filled with target gases (oxygen or hydrogen) with absolute pressure around 70 psi and then the whole system is isolated. The pressure increase of the permeate side is monitored via a pressure transducer. Since the feed side is connected with a large buffer vessel (500 cm^3), the pressure decrease of the feed side during permeation is less than 1 %, which can be ignored. As the feed side is under low pressure (below 500 mTorr), ideal gas law can be applied to calculate the gas permeance

$$P_x = \frac{dp_p}{dt}\frac{V}{RTA(p_F - p_p)} \approx \frac{dp_p}{dt}\frac{V}{RTAp_F} \quad \text{(Eq S19)}$$

P_x is the permeance (x = oxygen or hydrogen), p_F is the absolute pressure of feed side, p_p is the absolute pressure of permeate side, $\frac{dp_p}{dt}$ is the pressure increasing rate of permeate side, V is the total volume of the permeate side, R is the gas constant, T is the system temperature (35 °C), and A is the exposed membrane area.

After permeation measurement, the membrane is disassembled from the membrane cell. The exposed membrane area, A, and the membrane thickness, l, are measured. Permeability, $\mathbb{P}_x$, can be calculated via the following equation

$$\mathbb{P}_x = P_x l \quad \text{(Eq S20)}$$

Note S5. Mechanical characterizations of optofluidic probe.

All the mechanical properties in figs. S3 and S6 are measured on RSA-G2 (TA Instruments) dynamic mechanical analyzer. The stress-strain curves of the SBS film and the optofluidic probe are measured in the tension mode. The sample is clamped between the top and bottom of the cantilever in tension. The tensile modulus is calculated by fitting the tangent of the linear elastic region in the stress-strain curve. The bending stiffness is measured in the single cantilever mode with the oscillation frequency ramping from 0.1 to 10 Hz.

Note S6. Flow rate measurement.

The flow rate is measured by tracking fluorescent microbeads under high speed microscope (Nikon confocal microscope, CSU-W1). In the experiments, the fluorescent microbeads (1 wt% in DI water, FluoSpheres™ carboxylate-modified microspheres, 1.0 μm, yellow-green fluorescent (505/515)) is injected into the drug μ-reservoir. The tip of μ-fluidic channels is implanted into a hydrogel medium (0.6% agarose gel) to simulate *in vivo* environment. The delivery process is captured by high speed camera and the speed of microbeads is analyzed in ImageJ software.

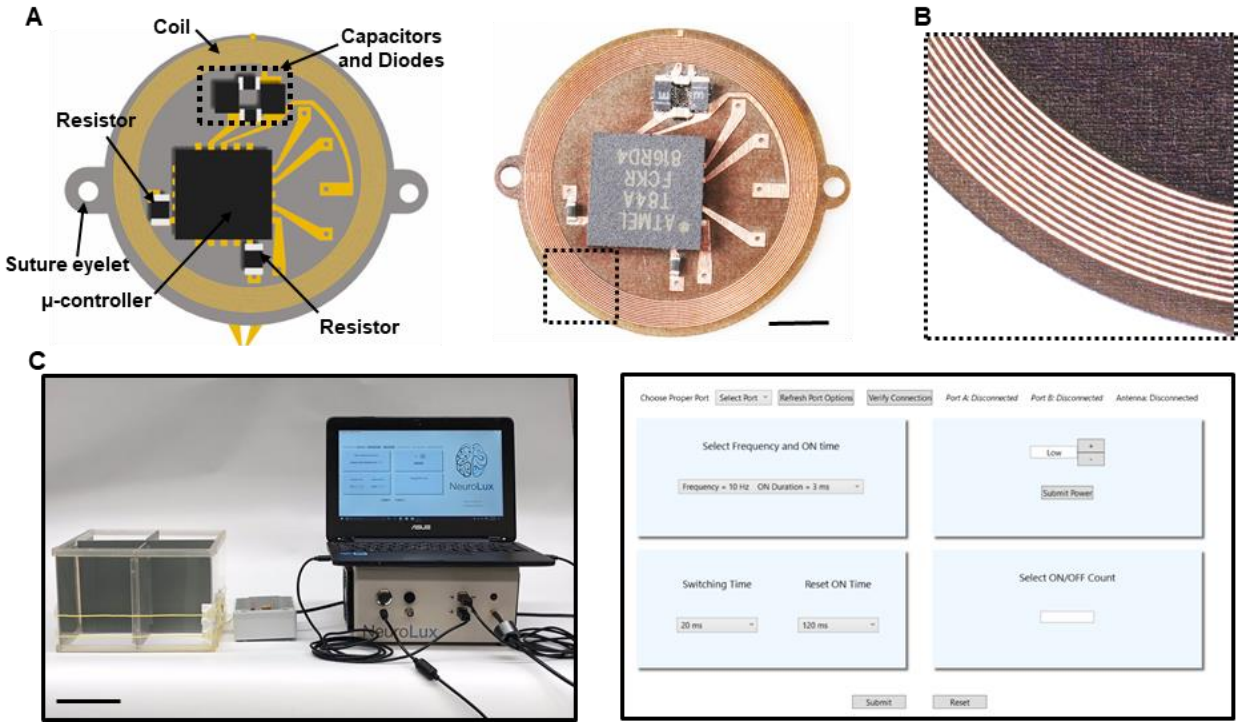

Fig. S1. Images of the wireless electronics and the complete system. (A), Bottom view of the schematic diagram in Fig. 1E and optical image of the device with mounted electronics, including capacitors, rectifiers, resistors, and μ-controller (Scale bar 0.2 cm). **(B)**, Enlarged optical image of the receiver coil. **(C)**, Picture of the external hardware (left) and screen images (right) from a customized software application as a user interface (Scale bar 10 cm). (Photo credit for part C: Aaron D. Mickle, Washington University in St. Louis).

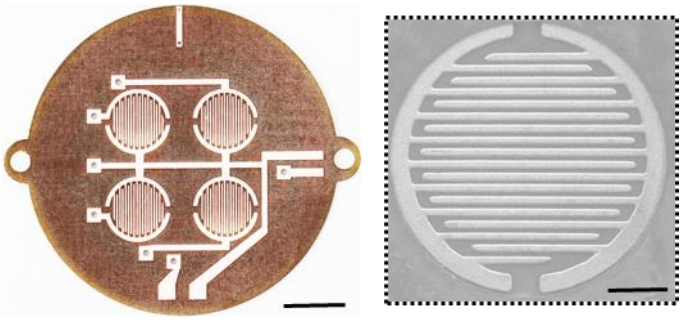

Fig. S2. Detailed images of the electrochemical micropump. Photographic image (left, Cu electrodes) and scanning electron microscope image (right, Au/Cu electrodes) of interdigitated electrodes on the top of a flexible printed circuit board (Scale bars left: 0.2 cm; right: 500 µm).

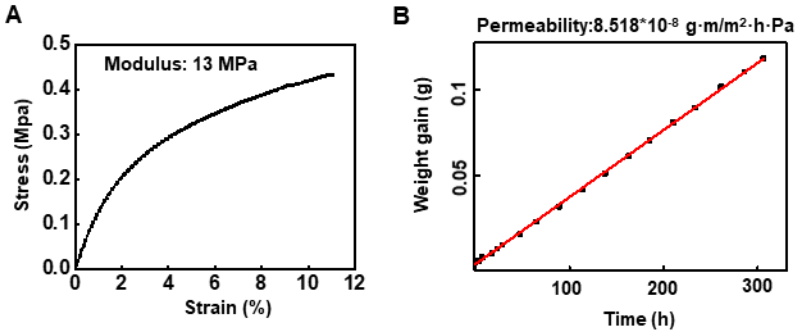

Fig. S3. Modulus and water permeability of the flexible SBS membrane. (A), Stress-strain curve of the SBS membrane (Modulus: 13 MPa). **(B)**, Water permeability measurements of the SBS membrane.

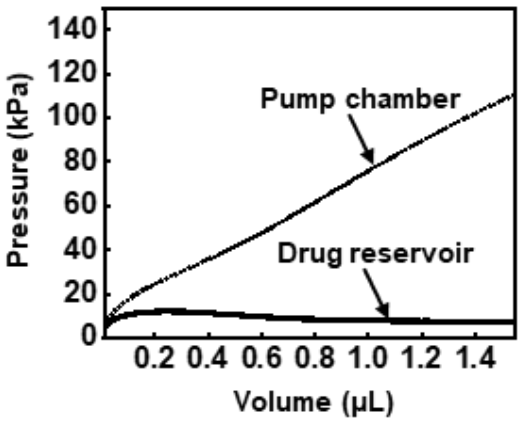

Fig. S4. Computational results for pressure in the pump chamber and the drug reservoir as a function of volume of drug delivered from the system.

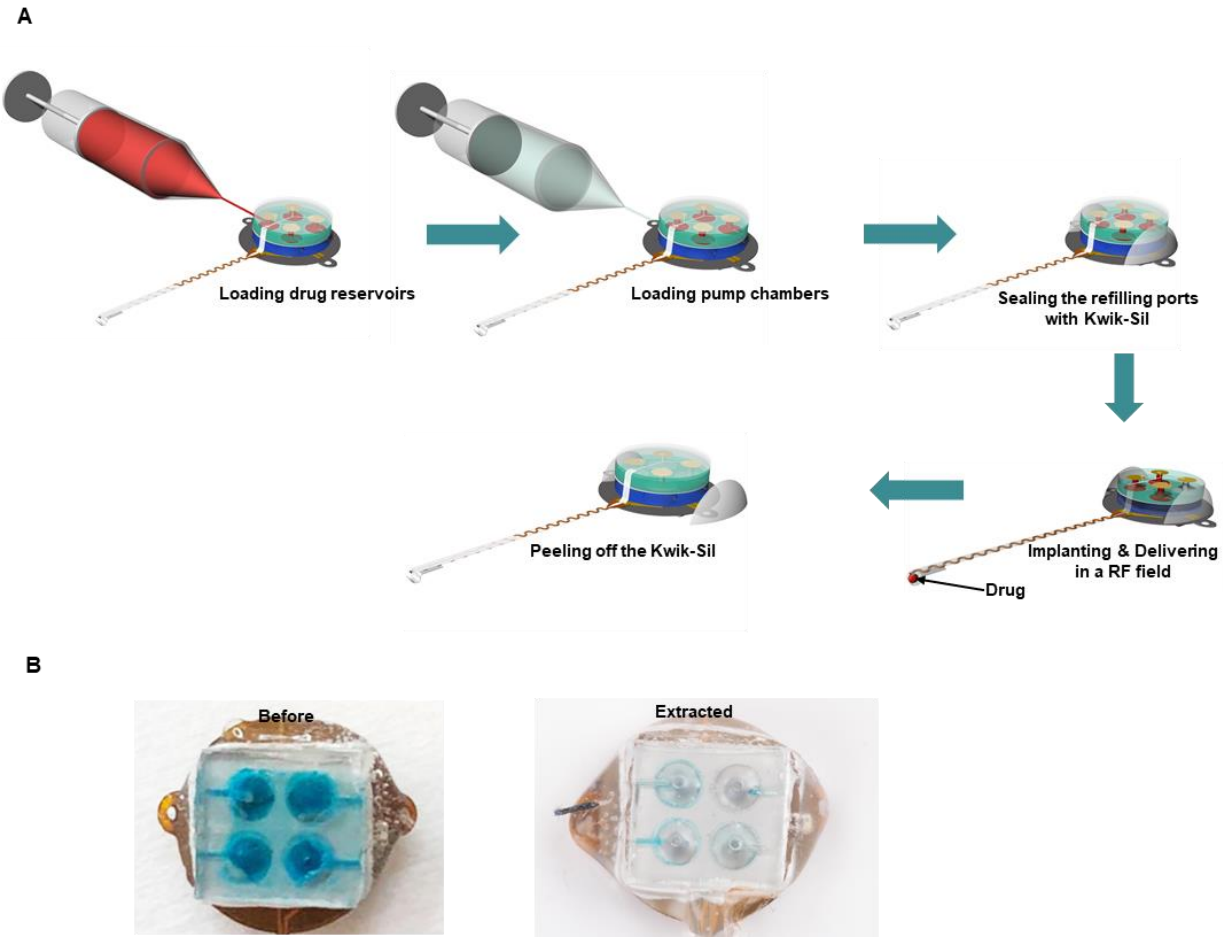

Fig. S5. Demonstration of drug loading and device reuse. (A), Schematic illustrations of the loading of drug reservoirs and pump chambers, sealing of the refilling ports, and reuse of the device. **(B)**, Photographic images of a wireless pump before implantation and extracted after the implantation. (Photo credit for part B: Yi Zhang, Northwestern University).

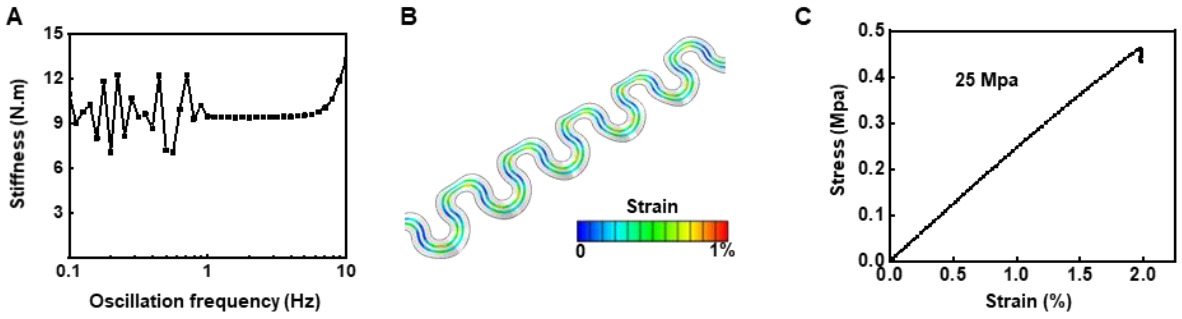

Fig. S6. Mechanical properties of the soft opotofluidic probe. (A), Bending stiffness of the optofluidic probe. **(B)**, Strain distribution of serpentine electrical interconnect under 15% stretch predicted by finite element analysis. **(C)**, Stress-strain curve of the optofluidic probe. Calculated modulus is 25 MPa.

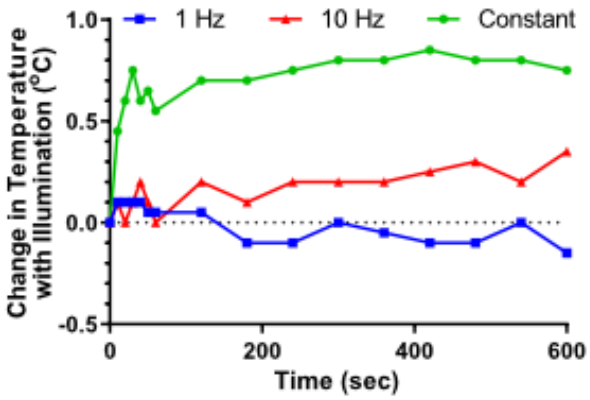

Fig. S7. Measurements of nerve temperature during various µ-ILED illumination protocols. *In vivo* measurements of sciatic nerve temperature adjacent to cuff implantation with illumination of the µ-ILED at different light pulse frequencies (1 Hz, 10 Hz, and constant illumination). At 1 and 10 Hz illumination (20 ms pulse width; 2.8 V) there was less than 0.3 °C change, and with constant illumination (2.8 V) there was less than 1 °C change in temperature of the nerve.

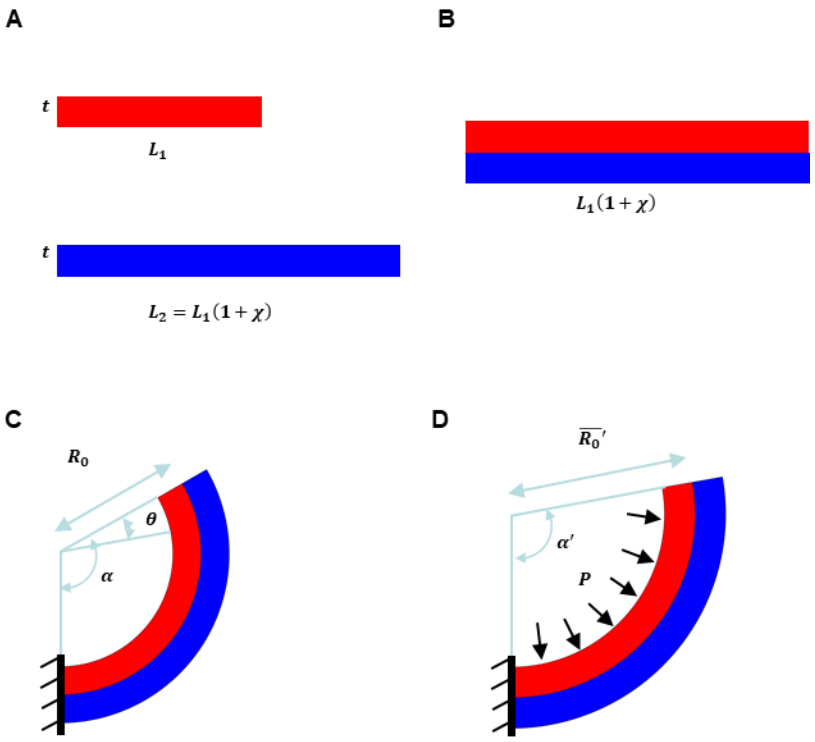

Fig. S8. Diagrams of formation of cuff from bilayer PDMS strips. (A), The initial geometries before applying pre-strain. **(B)**, The shorter strip (red) is stretched by pre-strain χ and the two strips are bonded together. **(C)**, The bi-layer system naturally forms a cuff with radius R_0 after releasing. **(D)**, After applying a uniform pressure P, the average radius of the cuff increased from R_0 to $\overline{R_0'}$.

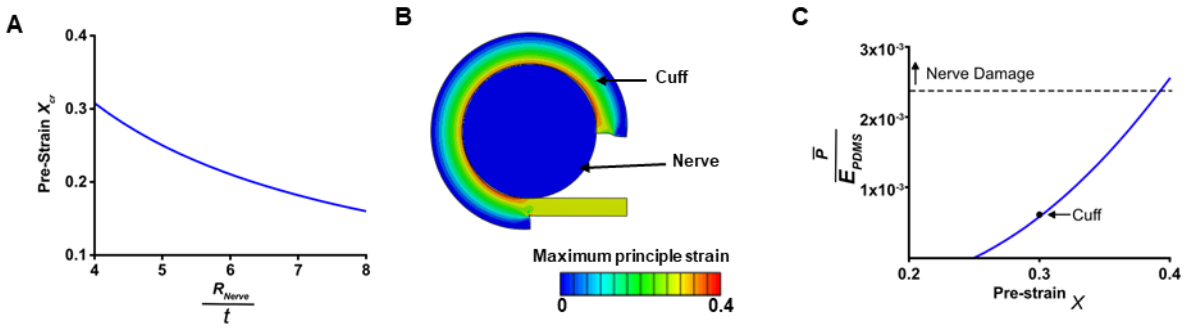

Fig. S9. Mechanical characterizations of cuff. (A), Critical pre-strain χ_{cr} required for the bi-layer PDMS trips to form a cuff with precise inner radius R_{Nerve}. (**B**), Finite element analysis (FEA) of the maximum principle strain distribution along the cuff-nerve interface. **(C)**, Estimated average contact pressure as a function of applied pre-strain χ.

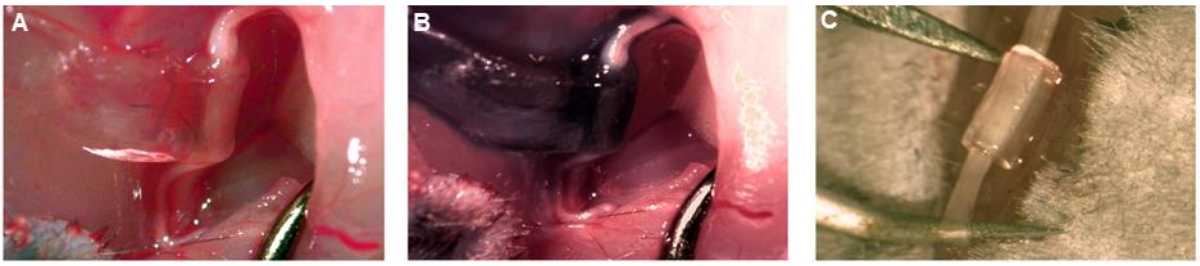

Fig. S10. Demonstration of the dye delivery via the optofluidic cuff 2 weeks after implantation and the positive control PE tubing cuff implantation. Representative images of the optofluidic cuff before **(A)** and after **(B)** blue dye delivery (6 µl) 2 weeks post-implantation, demonstrating functionality and durability of the system after chronic implantation. **(C)**, A 2 mm piece of PE-20 tubing with a vertical slit opening was implanted in a similar method to the optofluidic nerve cuff. This PE cuff is often used as a model for mild peripheral nerve crush injury.

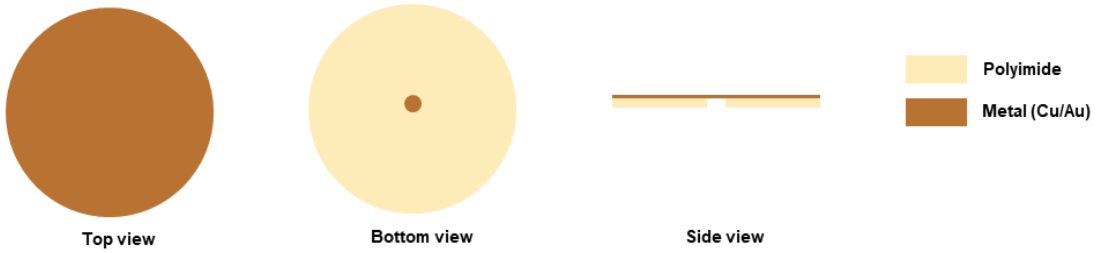

Fig. S11. Schematic illustrations of the metal membrane on the PI substrate.

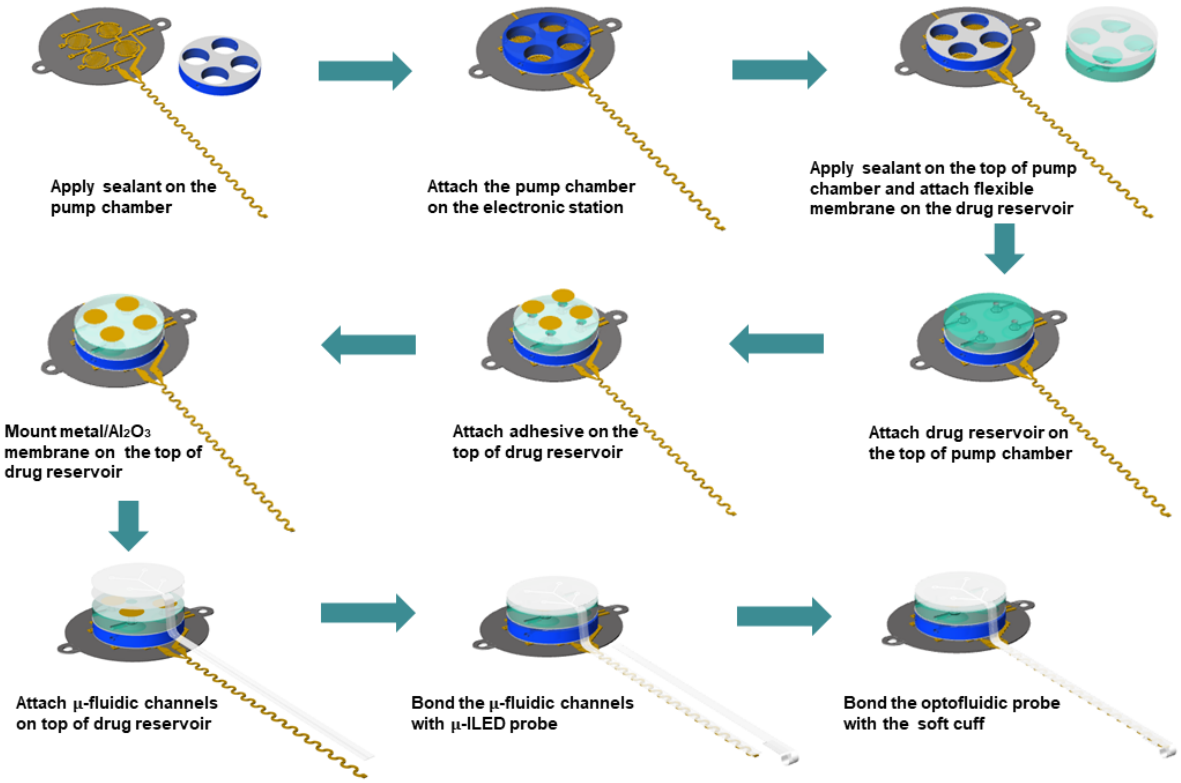

Fig. S12. Schematic illustrations of the assembly of device.

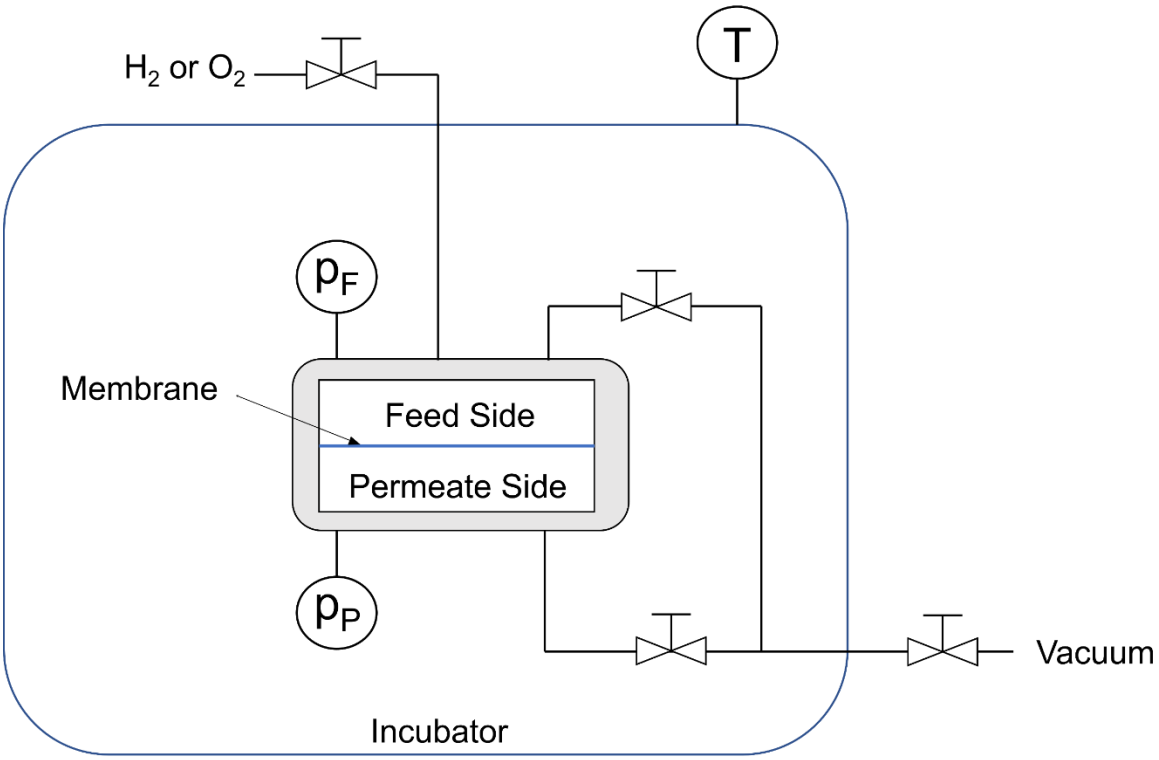

Fig. S13. Isochoric gas permeation system. Reproduced from the reference (*47*).

Table S1. Oxygen and hydrogen permeability of the flexible SBS membrane.

	Permeability （barrer）	Permeance (GPU)
Oxygen	**11.88**	**0.58**
Hydrogen	**21.66**	**1.06**

Table S2. Fabrication process details. * denotes the component from this fabrication step is reusable.

Process	Required time for 10 devices	Equipment	Note
Fabrication of the soft nerve cuff	7 hours	Spin-coater	
Fabrication of the microfluidic probe	10 hours	Cleanroom, mask aligner, spin-coater	
Fabrication of the µ-ILED probe	7 hours	Cleanroom, mask aligner, spin-coater, sputtering deposition	
Fabrication of the metal/Al_2O_3 membrane	7 hours	Cleanroom, mask aligner, spin-coater, E-beam deposition, ALD	
Fabrication of electronic base station	3 hours	ProtoLaser U4	*
Fabrication of the reservoirs and pump chambers	3 hours	CNC milling machine	*
Assembly of wireless electronics	2 hours	Solder, Microscope	*
Encapsulation (Parylene C)	5 hours	Parylene coater	*
Assembly of wireless µ-pumps	24 hours	Microscope	*
Bond microfluidic channels, µ-ILED probe, and soft cuff	10 hours	Microscope	
Encapsulation (PDMS)	1 hours	Oven	

Table S3. Statistical results for Fig. 3.

Figure #	Panel	n number	Error Bar	Statistical Test	Group	P Value	F	Degrees of Freedom
3	D	Sham n =9; Device n=10; PE cuff n=10	SEM	Two-way ANOVA with Tukey's multiple comparisons test	Sham - No device vs. Device	0.9506	9.503	2
					Sham - No device vs. PE Cuff	<0.0001		
					Device vs. PE Cuff	<0.0001		
	E	Sham n =9; Device n=10 PE cuff n=8	SEM	One-way ANOVA with Tukey's multiple comparisons test	Sham vs. Device	0.7274	9.943	2
					Sham vs. PE Cuff	0.0009		
					Device vs. PE Cuff	0.0044		
	F	Sham n =9; Device n=10 PE cuff n=8	SEM	One-way ANOVA with Tukey's multiple comparisons test	Sham vs. Device	0.5425	3.68	2
					Sham vs. PE Cuff	0.0101		
					Device vs. PE Cuff	0.0824		
	G	Sham n =9; Device n=10 PE cuff n=8	SEM	One-way ANOVA with Tukey's multiple comparisons test	Sham vs. Device	0.5255	5.337	2
					Sham vs. PE Cuff	0.0325		
					Device vs. PE Cuff	0.2251		
	I	n=3 all groups	SEM	One-way ANOVA with Tukey's multiple comparisons test	sham 2 weeks vs. device 2 weeks	0.9973	23.85	4
					sham 2 weeks vs. sham 10 weeks	>0.9999		
					sham 2 weeks vs. device 10 weeks	>0.9999		
					sham 2 weeks vs. PE cuff 2 weeks	0.0001		
					device 2 weeks vs. sham 10 weeks	0.9991		
					device 2 weeks vs. device 10 weeks	0.9991		
					device 2 weeks vs. PE cuff 2 weeks	0.0002		
					sham 10 weeks vs. device 10 weeks	>0.9999		
					sham 10 weeks vs. PE cuff 2 weeks	0.0001		
					device 10 weeks vs. PE cuff 2 weeks	0.0001		

Table S4. Statistical results for Fig. 4.

Figure #	Panel	n number	Error Bar	Statistical Test	Group	P Value	F	Degrees of Freedom
4	C	n= 10 C57 (10 hrtz and 1hrtz); n=9 TRPV1-chr2 (1 hz); n=8 TRPV1-chr2 (10 Hz)	SEM	Two-way ANOVA with Sidak's multiple comparisons test	C57 Vs TRPV1-Chr2 10Hz	0.0655	13.93	1
					C57 Vs TRPV1-Chr2 1Hz	0.0085		
	E	n= 6 (baseline and saline); n=5 Bupivicaine	SEM	One-way ANOVA with Sidak's multiple comparisons test	Ipsilateral - Baseline vs. Saline	0.2693	9.15	2
					Ipsilateral - Baseline vs. Bupivicaine	0.0424		
					Ipsilateral - Saline vs. Bupivicaine	0.0022		
		n= 6 (baseline and saline); n=5 Bupivicaine	SEM	One-way ANOVA with Sidak's multiple comparisons test	Contralateral - Baseline vs. Saline	0.7852	0.6817	2
					Contralateral - Baseline vs. Bupivicaine	0.4949		
					Contralateral - Saline vs. Bupivicaine	0.8615		